Nonlinear mountain waves in two and three spatial dimensions

By W. R. PELTIER   and   T. L. CLARK
Dept. of Physics, University of Toronto,
Toronto, Ontario M5S 1A7, Canada
National Center for Atmospheric Research,
Boulder, Colorado 80303, U.S.A.

Summary

A three-dimensional, time-dependent, anelastic model is employed to simulate the evolution of nonlinear internal waves which are forced by stratified flow over isolated topography. Both two-dimensional and three-dimensional flows are considered. In the former case the discussion focusses upon the development of the wave field induced by a uniform mean flow with constant stability. The full three-dimensional model is employed to study the nonlinear development of atmospheric 'ship-waves' which have recently been observed in satellite photographs to the lee of oceanic islands in the Norwegian and Barents seas. The model is able to reproduce the characteristics of the observed wave patterns rather nicely when it is initialized with vertical profiles of wind and stability obtained through upper air ascents from stations located on the islands themselves. Detailed comparisons of the output of the nonlinear model with the results of three-dimensional linear steady state theory are also provided. As is found to be the case in two-dimensional analyses, linear theory may considerably underestimate the forced wave amplitude for symmetric topographic excitation.

1. Introduction

In the past several years considerable new work has been undertaken on the old problem of internal waves forced by stratified flow over isolated topography. Motivation for this work has been provided by the recognition that such disturbances may be of crucial importance in understanding dynamical phenomena on a wide range of spatial scales. On the planetary scale, it has been suggested by Lilly (1972), based upon work by Sawyer (1959) and Bretherton (1969), that the drag exerted on the mean flow through the absorption of internal wave momentum flux could be the missing ingredient in the GCM which is required to explain why such models characteristically overpredict the strength of the mid-latitude jet stream. On the mesoscale, one direct stimulus to the revival of interest in these waves has been the recognition of their importance in the dynamics of severe downslope windstorms. Klemp and Lilly (1975) and Peltier and Clark (1979) have formulated alternative theories for the generation of such storms which are nevertheless both based upon the dynamics of internal waves. Even on the intermediate synoptic scale, the field of internal waves launched by topography might exert considerable influence on occasion. For example, the mechanism of lee cyclogenesis as described by Buzzi and Tibaldi (1978) and Steinacker (1979) appears to involve an initial slowing down of the cold front as it crosses the Alps (for example), which is followed by development of the upper-level trough prior to lee cyclone formation. It might be expected on the basis of the wave mechanical ideas discussed in Peltier and Clark (1979) that the internal wave field could play some role in the upper-level development.

The ALPEX experiment, which was conducted in the European Alps from 1 September 1981 to 30 September 1982, had among its objectives the collection of a detailed observational data set which can be employed to investigate the above mentioned processes. This geographic location is ideally suited to such an experiment both because of the high frequency of occurrence of lee cyclogenesis (the Genoa cyclone) and because of the frequency of local downslope windstorm occurrence (föhn, bora). The theoretical assimilation of the data which this experiment has produced will doubtless require the application of a wide variety of numerical models, optimally designed for the investigation of processes on various temporal and spatial scales. On the smallest temporal and spatial scales which are involved in downslope windstorm processes, non-hydrostatic effects are important and must be incorporated in the model if it is to be able to support, for

example, the vertical trapping of internal waves with horizontal spatial scales on the order of 10 km or so.

In the present paper we wish to describe a sequence of initial experiments with the nonlinear, non-hydrostatic, three-dimensional model which we intend to later apply to the analysis of ALPEX data. These experiments are designed to test the model against observational data in which the internal wave response to the topographic forcing is sufficiently simple geometrically that meaningful comparisons may be made. The data set which we have elected to investigate concerns a sequence of ship-wave patterns which were observed using the NOAA 5 satellite in the lee of islands in the Norwegian and Barents seas. The nature of the topographic forcing here ensures a relatively uncomplicated geometric response which may be simply compared to model output and which is of some intrinsic physical interest. The atmospheric analogue of the diverging and transverse patterns of surface gravity waves attached to a ship moving through deep water is supported by the topographic excitation of 'leaky' internal wave normal modes. Since the existence of such modes is entirely a consequence of non-hydrostatic effects, a test of the ability of the numerical model to reproduce observations of them constitutes a good test of the model's design.

In section 2 we provide a brief description of the structure of the time-dependent nonlinear numerical model and also of the linear steady state calculation which we have developed for comparison purposes. Section 3 is concerned with the discussion of a sequence of two-dimensional nonlinear simulations of the wave field launched in flows with uniform wind and stability. These calculations are intended to illustrate and to extend our previous results for circumstances in which no trapped wave exists but in which the nonlinear wave is of such large amplitude that it 'breaks'. Section 4 describes the observed ship-wave patterns and our simulations of them using both linear and nonlinear models. Concluding remarks will be found in section 5.

2. THE MODELS

(a) The nonlinear time-dependent model

The basic characteristics of the three-dimensional hydrodynamic model are described in detail in Clark (1977) and alterations of this code which have been made to fit specific requirements of the simulation of two-dimensional internal waves are discussed in Clark and Peltier (1977) and Peltier and Clark (1979). The model is anelastic and therefore based upon the following form of the continuity equation which guarantees, by neglect of the local time derivative of the density field, ρ, complete filtering of sound waves from the model system:

$$\nabla \cdot (\bar{\rho}\mathbf{u}) = 0. \tag{1}$$

Here $\mathbf{u}$ is the velocity field and $\bar{\rho}(\mathbf{r})$ is the initial density field which is taken as a hydrostatic function of height only. The momentum equation in the anelastic approximation is

$$\bar{\rho}\, d\mathbf{u}/dt = -\nabla p' - \rho'\mathbf{g} + \nabla \cdot \boldsymbol{\tau} \tag{2}$$

in which p' and ρ' are pressure and density fluctuations respectively such that

$$\left.\begin{array}{l} p = \bar{p}(z) + p'(\mathbf{r}, t) \\ \rho = \bar{\rho}(z) + \rho'(\mathbf{r}, t) \end{array}\right\} \tag{3a}$$

and

$$d\bar{p}/dz = -\bar{\rho}g. \tag{3b}$$

The deviatoric stress tensor τ in Eq. (2) is obtained from

$$\tau_{ij} = \bar{\rho} K_m D_{ij} \tag{4}$$

in which the deformation tensor is

$$D_{ij} = \partial_j u_i + \partial_i u_j - \tfrac{2}{3}\partial_{ij} \nabla \cdot \mathbf{u} \tag{5a}$$

with
$$
\begin{aligned}
K_m &= (k\Delta)^2 \,|\,\mathrm{DEF}\,|\,(1 - Ri)^{1/2}, &&\text{for } Ri < 1 \\
&= K_0 \text{ (small)}, &&\text{for } Ri \geq 1
\end{aligned} \tag{5b}
$$

where
$$(\mathrm{DEF})^2 = \tfrac{1}{2}(D_{11}^2 + D_{22}^2 + D_{33}^2) + D_{12}^2 + D_{13}^2 + D_{23}^2. \tag{5c}$$

Equations (1) and (2) are completed with an equation for conservation of internal energy in the form

$$\bar{\rho}\, d\theta/dt = \nabla \cdot \mathbf{H} \tag{6}$$

in which θ is the potential temperature and $\mathbf{H}$ is the heat flux vector defined by

$$\mathbf{H} = \bar{\rho} K_H \nabla \theta. \tag{7}$$

We always assume $K_m/K_H = 1$ and therefore that the eddy Prandtl number is unity. Equation (5b), which defines the eddy mixing coefficient for momentum, constitutes a first-order closure for the diffusive effects of turbulence in terms of the resolved fields. Although this is in no sense rigorous it does allow us to include mixing effects due to small-scale 'breaking' (convective instability) of a nonlinear wave when these small-scale effects are not fully resolved in the finite difference model. The connection between the thermodynamic fields p, ρ, θ is provided by the ideal gas equation of state and the definition of potential temperature, linearization of which gives

$$\rho' = -\bar{\rho}\,\theta'/\bar{\theta} + p'/\bar{c}^2 \tag{8}$$

where $\bar{c}^2 = \gamma R \bar{T}$ is the square of the adiabatic sound speed. The current version of the model has the background state $\bar{\rho}$, $\bar{p}$, $\bar{T}$, $\bar{\theta}$ determined by upwind rawindsonde data.

If one could usefully describe the phenomena of interest using a model written in Cartesian coordinates, the solution of Eqs (1), (2), (6) and (8) would be quite straightforward using well-established finite difference techniques. It is not possible to describe accurately the air flow over smooth topography in this fashion, however, and so we are obliged to employ a terrain-following coordinate system for the non-hydrostatic equations. We use the transformation

$$
\left.
\begin{aligned}
\bar{x} &= x \\
\bar{y} &= y \\
\bar{z} &= H\{z - z_s(x,y)\}/\{H - z_s(x,y)\}
\end{aligned}
\right\} \tag{9}
$$

to map the rectangular domain with bottom topography $z_s(x, y)$ into a regular parallelopiped. In Eqs. (9) H is the height of the numerical domain so that the coordinate system becomes Cartesian at this height. The analytic form of the model equations in the transform domain are given in Clark and Peltier (1977) and their numerical forms appear in Clark (1977). The model is time-stepped in the transform domain using second-order-accurate differencing and the transform domain solutions are inverted to physical space for analysis. Full numerical details will be found in the previously cited references.

(b) A spectral approach to the construction of linear steady state solutions

In Peltier and Clark (1979) we described a two-dimensional linear steady state model which was employed for comparison with output from corresponding nonlinear time-dependent analyses. That model was based upon a so-called multiple layer method in which the background atmosphere was approximated by a stack of layers in which the wind and temperature were assumed constant. Although such models are adequate for many applications they are by no means perfect and we have elected to do the linear

calculations to be reported here in a completely different manner. Retaining the full effects of compressibility for purposes of this linear analysis, the hydrodynamic fluctuations from the hydrostatic basic state $(\bar{\rho}, \bar{p}, \bar{T})$, in which the wind field, $U_{,} = (U, V, 0)$ with U and V functions of z only, are governed by the following perturbation equations

$$\partial u'/\partial t + U \, \partial u'/\partial x + V \, \partial u'/\partial y + w' \, \partial U/\partial z = -(1/\bar{\rho}) \, \partial p'/\partial x \qquad (10a)$$

$$\partial v'/\partial t + U \, \partial v'/\partial x + V \, \partial v'/\partial y + w' \, \partial V/\partial z = -(1/\bar{\rho}) \, \partial p'/\partial y \qquad (10b)$$

$$\partial w'/\partial t + U \, \partial w'/\partial x + V \, \partial w'/\partial y \qquad\qquad = -(1/\bar{\rho}) \, \partial p'/\partial z - \rho'g/\bar{\rho} \qquad (10c)$$

$$\partial \rho'/\partial t + U \, \partial \rho'/\partial x + V \, \partial \rho'/\partial y + w'\partial\bar{\rho}/\partial z + (\partial u'/\partial x + \partial v'/\partial y + \partial w'/\partial z) = 0 \qquad (10d)$$

$$\partial p'/\partial t + U \, \partial p'/\partial x + V \, \partial p'/\partial y + w'\partial p/\partial z -$$
$$- c^2(\partial \rho'/\partial t + U \, \partial \rho'/\partial x + V \, \partial \rho'/\partial y + w' \, \partial\bar{\rho}/\partial z) = 0 . \qquad (10e)$$

Solutions to Eqs. (10) are constructed using a spectral method by decomposing each of the hydrodynamic fields Ψ' into horizontal wavenumber and temporal frequency spectra through introduction of the three-dimensional Fourier integrals

$$\Psi'(k, l, z, \omega) = \iiint dx \, dy \, dt \, \exp\{-i(\omega t - kx - ly)\} \, \Psi'(x, y, z, t) \qquad (11a)$$

$$\Psi'(x, y, z, t) = (2\pi)^{-3} \iiint dk \, dl \, d\omega \, \exp\{i(\omega t - kx - ly)\} \, \Psi'(k, l, z, \omega) , \qquad (11b)$$

the integrals running from $-\infty$ to $+\infty$. Substitution of expansions of the form (11b) for each of the perturbation fields in (10) reduces this set of linear p.d.e.s to a set of coupled o.d.e.s for the complex spectral amplitudes $\Psi'(k, l, z, \omega)$. From this set of coupled o.d.e.s we may eliminate all the spectral amplitudes but one, say that for the vertical component of the velocity perturbation, $w'(k, l, z, \omega)$. This leads to a one-dimensional second-order o.d.e. which is analysed in detail in Simard and Peltier (1982). That paper also provides a detailed description of the numerical methods employed to reconstruct the linear steady state wavefield.

3. LARGE AMPLITUDE MOUNTAIN WAVES IN TWO DIMENSIONS

Our purpose in this section is to explore certain properties of highly nonlinear mountain waves in two dimensions. In Peltier and Clark (1979), we presented several nonlinear, time-dependent solutions for stratified flow over bell-shaped topography in an attempt to understand the detailed wave mechanical processes involved in the severe downslope windstorm which occurred at Boulder, Colorado on 11 January 1972. These calculations clearly established the importance of the breaking gravity wave to the dynamics of this event (also see Peltier and Clark 1980). One of the preliminary flows discussed in Peltier and Clark (1979) (and in Clark and Peltier 1977) was for the simple case of constant background wind and stability. For this example it proved to be rather difficult to separate the effects due to wave breaking from the effects due to the nonlinearity of the lower boundary condition. Our calculations did, however, show a significant departure from an approximate version of Long's model and since this model is supposed to account exactly for the effect of the nonlinear lower boundary condition we did find some indication that effects due to wave breaking could be quite important even in the simplest flows. Our intention here is to demonstrate in an unambiguous way that the same self-induced resonance invoked to account for downslope windstorms in more complicated models also seems to occur in flows with constant background wind and stability.

(a) Design of the numerical experiments

In order to separate boundary condition from breaking wave effects we have performed a sequence of numerical experiments which are somewhat different from those described in Peltier and Clark (1979). With u and w the horizontal and vertical components of the flow velocity, we previously employed the conditions

$$u = U_0 \quad \text{and} \quad \partial w/\partial x = \partial \theta/\partial x = 0 \tag{12}$$

at the inflow boundary of the two-dimensional domain. In the present experiments Eqs. (12) have been replaced by

$$\left. \begin{array}{l} \Theta = \Theta_0(z) \\[2mm] w = 0 \\[2mm] u = u(t). \end{array} \right\} \tag{13}$$

The time dependence of $u = u(t)$ at the inflow boundary is determined using a modification of the extrapolation scheme of Orlanski (1976) in which the tendency of u is taken proportional to

$$\Delta u = u^{\tau+1} - u^{\tau-1} = (1 - \varepsilon)\,\Delta u^* + \varepsilon(U_o - u^{\tau-1}), \tag{14}$$

in which Δu^* is determined using the Orlanski scheme. The choice $\varepsilon > 0$ in (14) limits the memory at the inflow boundary by continually forcing the solution back towards the initial state. If the internal forcing associated with upstream propagating modes changes scale with time then (14) allows the inflow boundary to adjust. A value of $\varepsilon = 0.025$ was employed in all the experiments to be described in this section. It is important to note that upstream blocking should not be important in any of the flows to be considered here since $U_0 > Nz_{s,\,max}$.

The main new feature of these experiments is that they are designed to investigate the response of the model to accelerations and decelerations of the fluid flowing through the upstream boundary. As we will show, such analyses will allow us to separate breaking wave from boundary condition effects. In order to impose such an acceleration we modify (14) for the period of flow transition to the form

$$\Delta u \rightarrow \Delta u + q\,\Delta U_0 \tag{15}$$

in which ΔU_0 is the desired net change in the mean flow speed U_0 and q is selected such as to make acceleration constant over the transition period. When (15) is applied to the elliptic pressure equation (see Clark and Peltier 1977) the flow transition is smooth and the governing equations are satisfied at all times in the domain interior.

(b) Description of the two-dimensional experiments

In all the experiments to be discussed here we have employed bell-shaped topography z_s given by

$$z_s(x) = ha^2/(x^2 + a^2) \tag{16}$$

with $h = 400\,\text{m}$ and $a = 3\,\text{km}$. The static stability $S = d(\ln\theta_0)/dz = 10^{-7}\,\text{m}^{-1}$ is fixed, which implies a Brunt–Väisälä frequency $N = 0.99 \times 10^{-2}\,\text{s}^{-1}$ with corresponding period $\tau_N = 10.57\,\text{min}$. If the flow were hydrostatic then we know that flow over the obstacle would generate internal waves with vertical wavelength $\lambda_z = 2\pi U_0/N$. This vertical wavelength is $2.54\,\text{km}$ for $U_0 = 4\,\text{m s}^{-1}$ and $3.17\,\text{km}$ for $U_0 = 5\,\text{m s}^{-1}$. Miles and Huppert (1969) have shown that so long as the Froude number $Fr = hN/U_0$ is in the range $0 \le Fr < 0.85$ then the internal waves generated by flow over the bump will not be supercritically steepened (i.e. will not break). Their calculation includes the full effect of the nonlinear lower boundary condition as it is based upon Long's model. Since the

choice $U_0 = 5 \, \text{m s}^{-1}$ gives $Fr = 0.7924$ and the choice $U_0 = 4 \, \text{m s}^{-1}$ gives $Fr = 0.9905$ it is quite clear that the former case will be subcritical and the latter case supercritical with respect to wave breaking.

Since the model which we employ has the capacity to trace the evolution of the flow in response to an acceleration we are thus able to investigate the transition between these two states. What we shall do is to set up a steady wave field in the subcritical state with $U_0 = 5 \, \text{m s}^{-1}$ and then decelerate to $4 \, \text{m s}^{-1}$, which will induce wave breaking. As we will show this leads to a marked *increase* of the surface wave drag in circumstances in which Long's model predicts that the drag should *decrease*. It is in this way that we are able to distinguish effects due to the nonlinear lower boundary condition which are contained in Long's model and effects due to wave breaking.

Our computations of surface wave drag in these experiments have been done using the expression

$$D_w(0) = -\int_{-\infty}^{+\infty} p'(\partial z_s/\partial x) \, dx \tag{17}$$

in which p' is the pressure perturbation and z_s is the topography as before. In Clark and Peltier (1977) our calculations of the interior Reynolds stress profile did not match the wave drag at the ground given by (17) as they should have done. In that paper we calculated Reynolds stress as a function of height by linearly interpolating ρ, u' and w' separately to common height levels prior to horizontal averaging to obtain $\langle \rho u'w' \rangle$. An
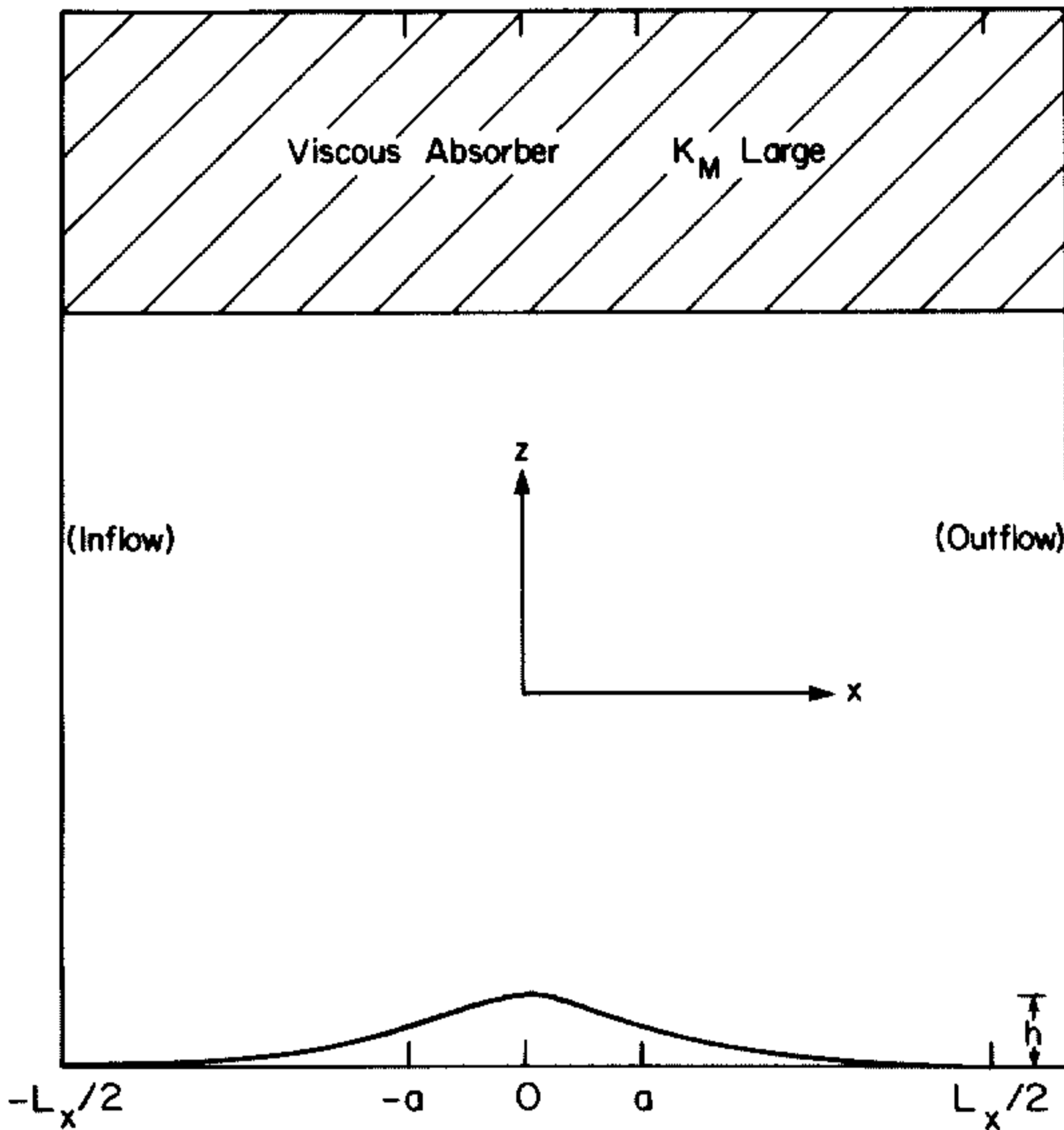

Figure 1. Schematic of the numerical domain. Note the presence of the region of viscous absorption adjacent to the upper boundary.

artifact of this approach is the $3\Delta z$ anomalous structure in $\langle\rho u'w'\rangle$ near the surface and the mismatch with Eq. (17). Here we have alleviated this problem by first calculating ρuw on the transformed grid and then interpolating to constant height levels to obtain $\langle\rho u'w'\rangle = \langle\rho uw\rangle - \rho UW$ with $U = \langle u\rangle$ and $W = \langle w\rangle$. This procedure has solved the previous problem of the mismatch between the interior wave momentum flux and the surface wave drag.

In Fig. 1 we illustrate the domain in which the numerical experiments to be described in this section have been performed. Before discussing the main sequence of calculations it is important to understand in advance one characteristic of the general class of simulations with accelerated mean flows. This involves the sensitivity of the final wave states to high frequency noise generated during mean flow acceleration and the dependence of the amplitude of this noise on the time scale over which the acceleration occurs. In (a) and (b) of Fig. 2 we show vertical velocity fields for two experiments after an integration time of
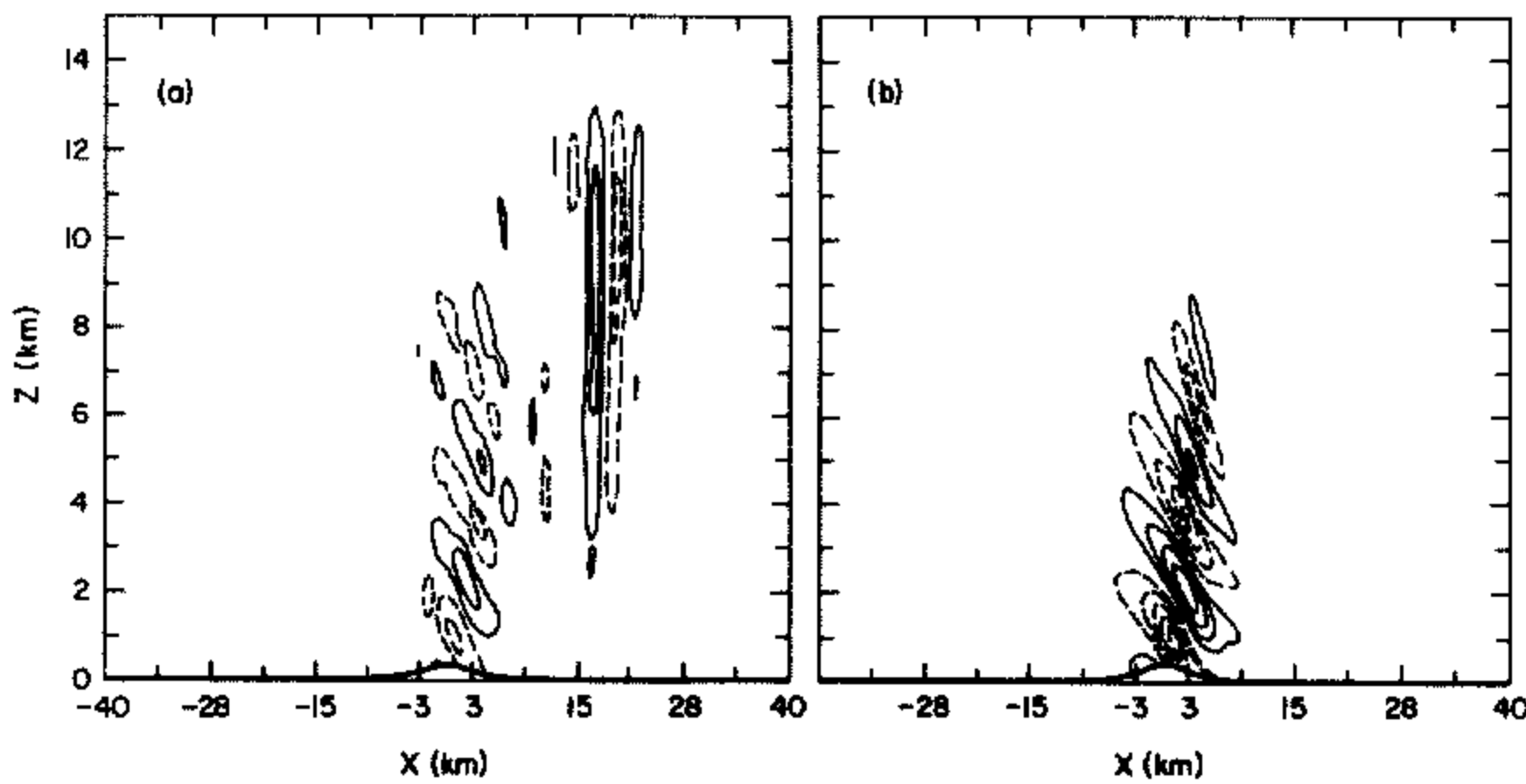

Figure 2. Vertical velocity fields at $t = 100$ min for experiments 29, (a), and 30, (b). The contour intervals are $0.3125\,\mathrm{m\,s^{-1}}$ and $0.1562\,\mathrm{m\,s^{-1}}$ in (a) and (b) respectively. Solid contours denote positive values and dashed contours denote negative values.

100 min. Both these experiments investigate the wave fields generated by mean flows of strength $U_0 = 5\,\mathrm{m\,s^{-1}}$ but differ in the time scale over which this steady mean flow is established from the initial state of rest. In Fig. 2(a) the mean flow acceleration takes place over a time $10\,\Delta t = 0.24\,\tau_N$, whereas in Fig. 2(b) the acceleration time is $200\,\Delta t = 4.73\,\tau_N$. As illustrated in Fig. 2 the final wave states for the case with rapid initial acceleration are strongly contaminated by high frequency noise whereas the simulation with more gradual acceleration is free of such undesirable influence. In order to suppress the generation of undesirable high frequency noise in experiments with accelerated mean flow, acceleration periods are constrained to be significantly in excess of the buoyancy period, τ_N. Figure 3 provides a further illustration of this in the form of histories of surface wave drag computed from Eq. (17) for the same two experiments. Curve 30 is the drag curve for slow acceleration; curve 29 for rapid acceleration. The latter shows clear evidence of the high frequency noise generated during startup, which obviously persists through the integration period. Both experiments were conducted on a finite difference grid with dimensions $136\,\Delta x$ by $92\,\Delta z$ with $\Delta z = 158.6\,\mathrm{m}$ and an overhead absorber depth of $40\,\Delta z$. Figure 4 illustrates the temporal evolution of the Reynolds stress profile for this flow with slow startup but with 192 vertical gridpoints, $\Delta z = 79.3\,\mathrm{m}$, and an overhead absorber depth of $80\,\Delta z$. Such data are typical of all model runs with the model running in subcritical conditions (in this case $Nh/U_0 = 0.792$) and shows that in the long-time limit the Rey-
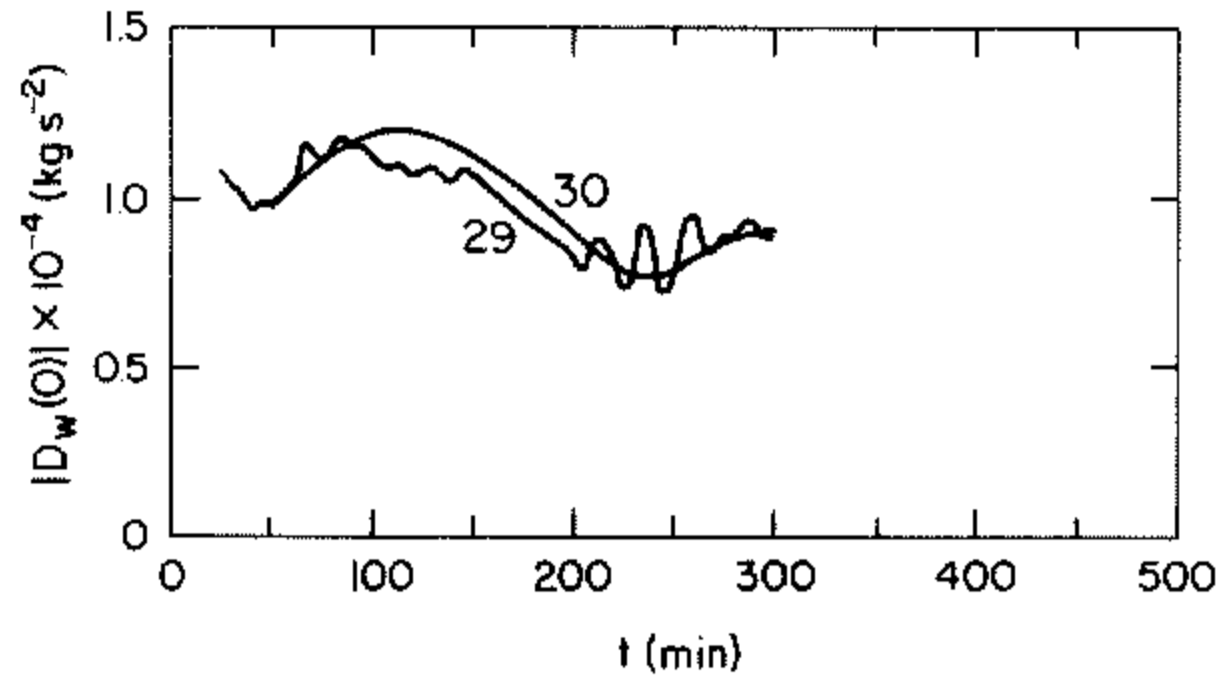
Figure 3. Surface wave drag as a function of time for experiments 29 and 30. Note the high frequency noise contaminating the drag curve for experiment 29 which is produced by the shock startup.
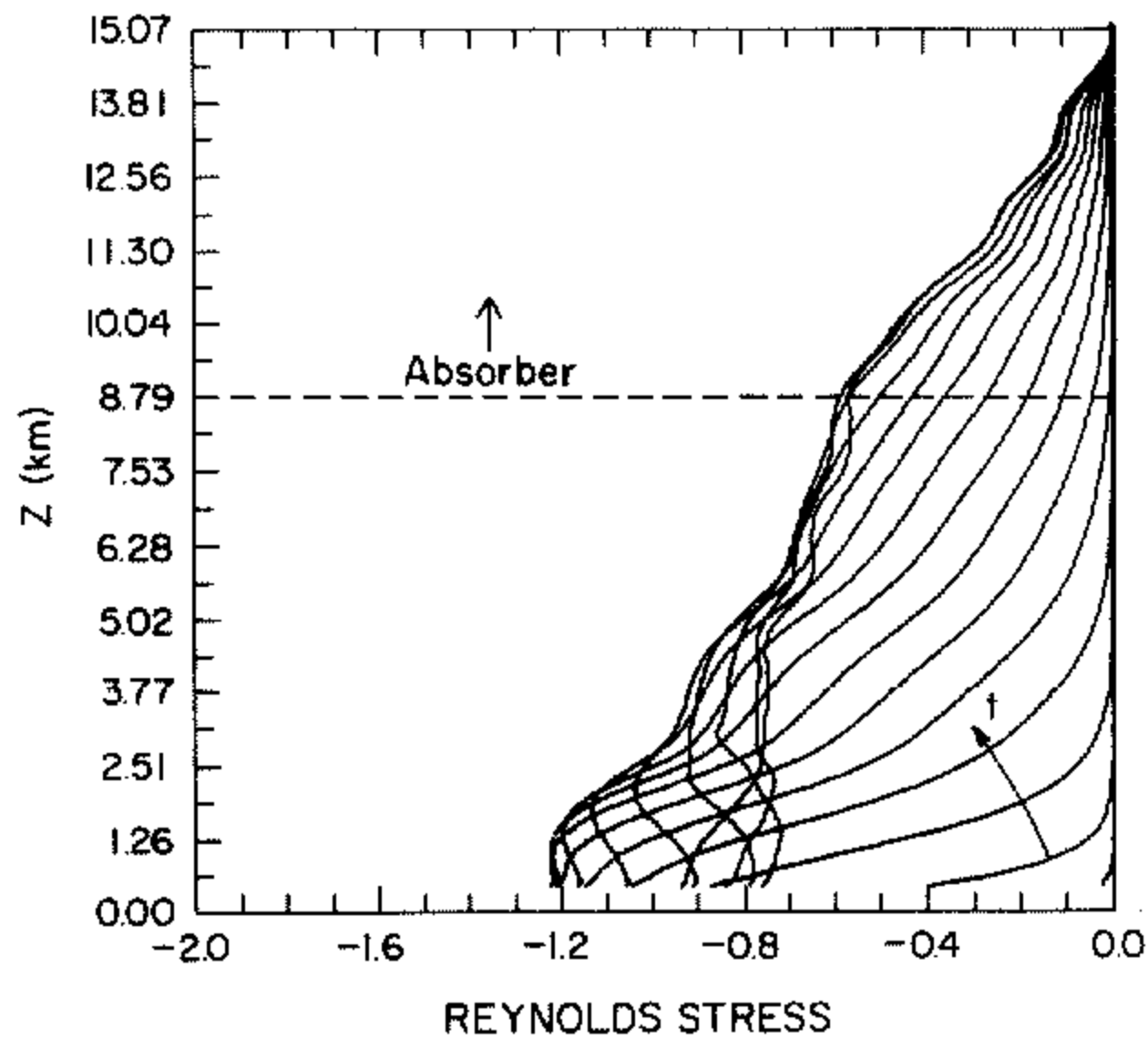

Figure 4. Reynolds stress profiles for experiment 37. The arrow shows time progressing and individual profiles are drawn at 20 min intervals. Note that the concentrated group of profiles, which are for the latest time shown, are characterized by nearly constant Reynolds stress in the region beneath the viscous absorber.

nolds stress profile becomes constant in the region beneath the viscous absorber as expected on the basis of the Eliassen–Palm theorem.

Of the several new experiments which have been conducted to investigate the importance of wave breaking by decelerating a subcritical mean flow into the supercritical regime we will describe two examples here. In both experiments, 34 and 36, we first accelerated the mean flow from 0 to $5 \, \text{m s}^{-1}$ over a time of 50 min, kept the mean flow constant in this subcritical state until elapsed time $t = 135 \, \text{min}$, and then decelerated to $U_0 = 4 \, \text{m s}^{-1}$. The two experiments differ only in vertical resolution. Exp. 34 has 97 vertical gridpoints and $\Delta z = 153 \cdot 6 \, \text{m}$ while Exp. 36 has 192 vertical gridpoints and $\Delta z = 79 \cdot 3 \, \text{m}$. Figure 5 shows $D_w(0)$ v. t for these two experiments and illustrates the fact that wave drag increases dramatically in the supercritical state ($U_0 = 4 \, \text{m s}^{-1}$) even though Long's model, and linear theory, predict that the drag should decrease. Inspection of the figure shows that this effect is only enhanced by increasing the vertical resolution of the numerical model.
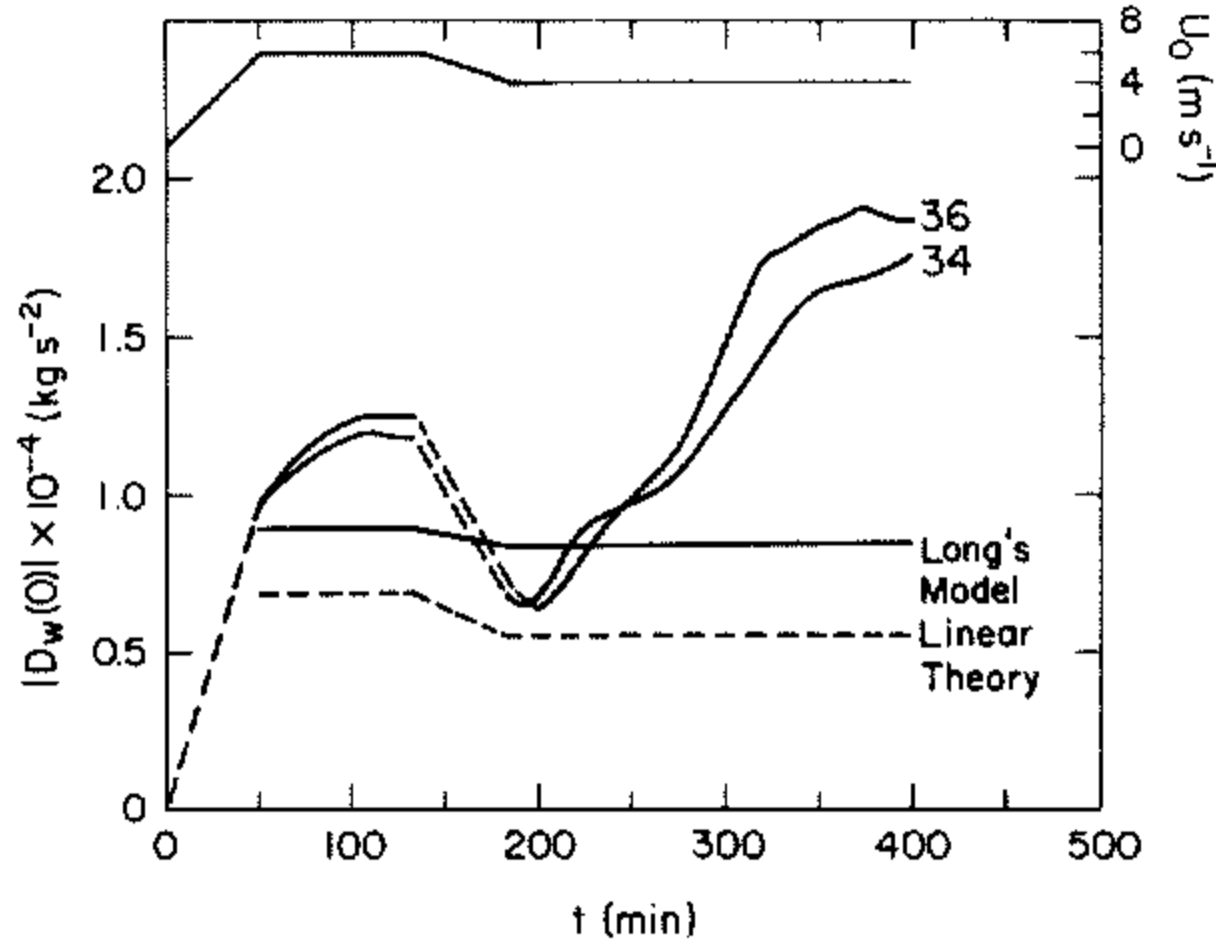
Figure 5. Plots of the surface wave drag $D_w(0)$ as a function of time for experiments 34 and 36. These plots illustrate the marked increase of wave drag which is produced when the internal wave is forced to break. The strength of the mean flow $U_0(t)$ is also shown on this figure for convenience. The breaks in the drag curves correspond to the time during which the flow is decelerated from a subcritical speed of $5\,\mathrm{m\,s^{-1}}$ to the supercritical speed of $4\,\mathrm{m\,s^{-1}}$.

Insight into the nature of the dynamical processes which support the transition from the low drag subcritical state, in which Long's model provides an adequate description of the flow, to the high drag state in which Long's model is completely inadequate is provided by Fig. 6. This shows a time sequence of interior Reynolds stress profiles for the
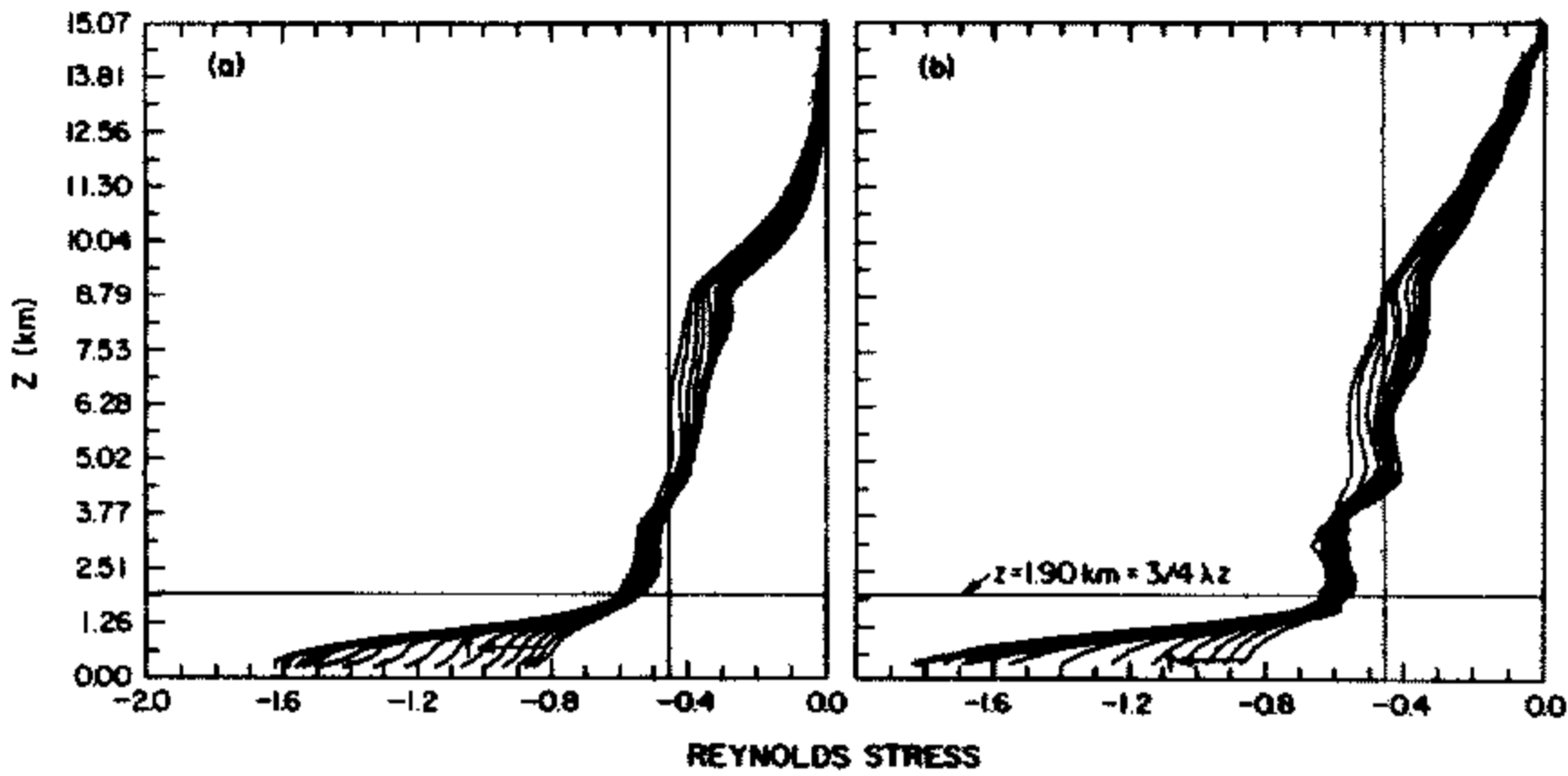

Figure 6. Composite Reynolds stress profiles for experiments 34, (a), and 36, (b). Note the sharp hinge at height $z = 3\lambda_z/4$. Time increasing is shown by the arrows on the bottom of each plate. The first profile drawn in each case is at time $t = 230\,\mathrm{min}$. The vertical line in each frame represents the critical Reynolds stress associated with a mountain height (forcing) just sufficient to cause the streamlines to steepen to vertical. The sharp stress drop above about $8.8\,\mathrm{km}$ altitude is due to the presence of the viscous absorber.

low resolution calculation, (a), and the high resolution calculation, (b). These profiles all match the corresponding $D_w(0)$ at the surface and have been drawn at 10-minute intervals beginning at $t = 230\,\mathrm{min}$. The important feature to note in both these sequences of profiles is the sharp ledge which develops at a height z which is precisely a distance $3\lambda_z/4$ above the ground, where λ_z is the vertical wavelength of the field of internal waves. As

shown in Peltier and Clark (1979) this is the height at which critical steepening first occurs and streamlines overturn. Systematic analysis of the streamfield data shows it is following the time at which critical steepening first occurs that the Reynolds stress profile begins to diverge strongly in the region between the ground and the height $3\lambda_z/4$. After supercritical steepening of the internal wave occurs the momentum flux above the steepening level, $3\lambda_z/4$, remains constant but beneath this level it diverges strongly. This is not in accord with the predictions of the Eliassen–Palm theorem but this theorem holds only for small amplitude steady state disturbances. Our interest here is in those large amplitude unsteady processes which occur in consequence of wave breaking.

The numerical data shown in Fig. 6 clearly imply that all wave energy incident from below on the level $3\lambda_z/4$, and in excess of that required to keep the streamlines at critical steepness, is not transmitted through this level. The vertical lines drawn at $D_w(0) = -0.45$ kg s^{-2} on both (a) and (b) thus represent the drag calculated from Long's model for the critical state in which $Fr = 0.85$. Wave energy reflected from the critical height is trapped in the cavity between this level and the ground with the total disturbance in this region growing continuously as a function of time. In a sense the field of internal waves seems to excite a 'self-resonance' when it is forced to exceed supercritical steepness. Precisely how this mechanism operates remains somewhat obscure. Our inability as yet to describe the process in terms of an analytically tractable model does not, however, detract at all from the importance of the process itself. It is exactly this process which we were obliged to invoke in Peltier and Clark (1979) to understand the ability of our model to reproduce the observations of the 11 January 1972 severe downslope windstorm at Boulder, Colorado.

A semi-quantitative understanding of the proposed resonant amplification process may be gained through the following argument. Assume that a certain basic wave disturbance of precisely critical amplitude has been established over the mountain and that this disturbance is essentially hydrostatic. The critical amplitude is that which leads to a streamline which is precisely vertical at the first steepening level. This steady state disturbance may be calculated from the hydrostatic version of Long's model or using the finite difference code, the main point being that the effect of the nonlinear lower boundary condition is included. Suppose that the height of the mountain is now increased from the critical height, h_c, to a new height h with all other parameters of the model fixed. We enquire as to the slow time scale transient evolution of the additional disturbance under the assumption that it is perfectly reflected from the critical region at height $3\lambda_z/4$. Except for the effect of reflection from the critical region, the disturbances may be linearly superimposed and the additional disturbance beneath the critical region will satisfy the evolution equation

$$\partial^4 \tilde{W}/\partial t^4 + k^2 c^2 \, \partial^2 \tilde{W}/\partial t^2 + k^2 c^2 N^2 \tilde{W} - c^2 \, \partial^4 \tilde{W}/\partial z^2 \partial t^2 - g\gamma \, \partial^3 \tilde{W}/\partial z \partial t^2 = 0 \qquad (18)$$

where $\tilde{W} = \rho_0 \tilde{w}$ and $\tilde{w}$ is the vertical component of perturbation velocity in the horizontal wavenumber domain. Equation (18) is for a fully compressible atmosphere and applies in the frame of reference in which the mean wind speed is zero. In the low frequency hydrostatic approximation which concerns us here (18) reduces to

$$\partial^4 \tilde{W}/\partial z^2 \partial t^2 - k^2 N^2 \tilde{W} = 0, \qquad (19)$$

where the Boussinesq approximation has been assumed.

We may solve (19) subject to the boundary conditions (i): $\tilde{w} = w_0 \exp(-i\omega t + ikx)$ on $z = 0$ (the ground) and (ii): perfect reflection at $z = 3\lambda_z/4$. (i) implies that we are restricting consideration to sinusoidal topography, not a strong constraint since the disturbance is hydrostatic. Since we are interested in growth on a slow time scale the wave frequency $\omega = kU = Nk/m$, where m is now the vertical wavenumber and k the horizontal wavenumber. If we transform to a new coordinate system in which the ground is located at $z = -d$ and the critical region at $z_c = d/2$ so that $d = \lambda_z/2 = \pi/m$, then the solution to the initial boundary value problem posed by Eq. (19) subject to (i) and (ii) above may be written in the form (Landau and Lifshitz 1960; p. 62)

$$\tilde{w} = \{at \sin(mz) + b(z - \tfrac{1}{2}d) \cos(mz)\} \exp(-i\omega t). \tag{20}$$

Substituting Eq. (20) into Eq. (19) we confirm that (20) is a solution if

$$i\omega m^2 a + 2\omega^2 mb = 0 \tag{21}$$

and if a and b are such that the lower boundary condition is satisfied. On $z = -d$, $\sin(mz) \equiv 0$ and satisfaction of the lower boundary condition demands

$$b = w_0/(\tfrac{3}{2}d). \tag{22}$$

This determines the growth rate, a, of the field $\tilde{w}$ uniquely from Eq. (21) as

$$a = (2i\omega/m)b. \tag{23}$$

From Eqs. (22) and (23) it is clear that the growth rate a depends upon the degree of supercriticality of the forcing $(h - h_c)$ through w_0 which is the supercritical amplitude of the vertical velocity at the lower boundary.

Inspection of Eq. (20) shows that $\tilde{w}$ is *not* a function of time on the lower boundary since $\sin(mz) \equiv 0$ there. However, this does not imply that the perturbation horizontal velocity is also stationary. From the Boussinesq form of the continuity equation we have

$$\tilde{u}^1 = -(1/ik)(\partial w/\partial z). \tag{24}$$

From Eq. 20 it therefore follows that

$$\tilde{u}^1 = -(1/ik)\{mat \cos(mz) - mb(z - \tfrac{1}{2}d) \sin(mz) + b \cos(mz)\} \tag{25}$$

and on the lower boundary becomes

$$\tilde{u}^1(z = -d) = (mat/ik + b/ik), \tag{26}$$

which shows that the perturbation horizontal velocity on the surface will increase linearly as a function of time although the vertical component of velocity remains stationary. Thus $D_w(0) = \langle \rho_0 u^1 w^1 \rangle$ will also be a linearly increasing function of time and this is in accord with the result of the numerical calculations shown in Fig. 6 for the Reynolds stress profiles. The instability behaves in a way which is completely analogous to that of a classical oscillator which is forced at its resonant frequency – the amplitude of the response increases linearly with time. The few calculations discussed here serve to illustrate that even the simplest two-dimensional mountain wave problem exhibits extremely interesting effects when the wave amplitude is sufficiently large. In the following section we will proceed to analyse some of the complexities which the added complications of three dimensionality and of structure in the mean flow can produce when they are combined.

4. ATMOSPHERIC SHIP-WAVES: LINEAR AND NONLINEAR SIMULATIONS

Gjevik and Marthinsen (1978) and more recently Marthinsen (1980) have presented and discussed several observations of atmospheric ship-wave patterns. Their data set will be employed here to test the ability of the nonlinear numerical model to reproduce such complex internal wave disturbances. Figure 7 displays, in (a), (b) and (c), three of the satellite photographs discussed in these papers and compares them in (d) with a photograph of ship-waves taken from Stoker (1957, Fig. 8.2.4, page 230). Inspection of (d) shows that the usual field of ship-waves consists of both diverging and transverse phase fronts. The atmospheric observations in (b) and (c) reveal rather pronounced diverging bow wave patterns whereas close analysis of (a) shows a wave field dominated by the transverse response. Our task here will be to determine whether the models discussed in section 2 are able to reproduce these observations when they are properly initialized.

Figure 8 shows the observed wind and temperature profiles for the three observational data sets which are required for initialization. Also included on these plates are
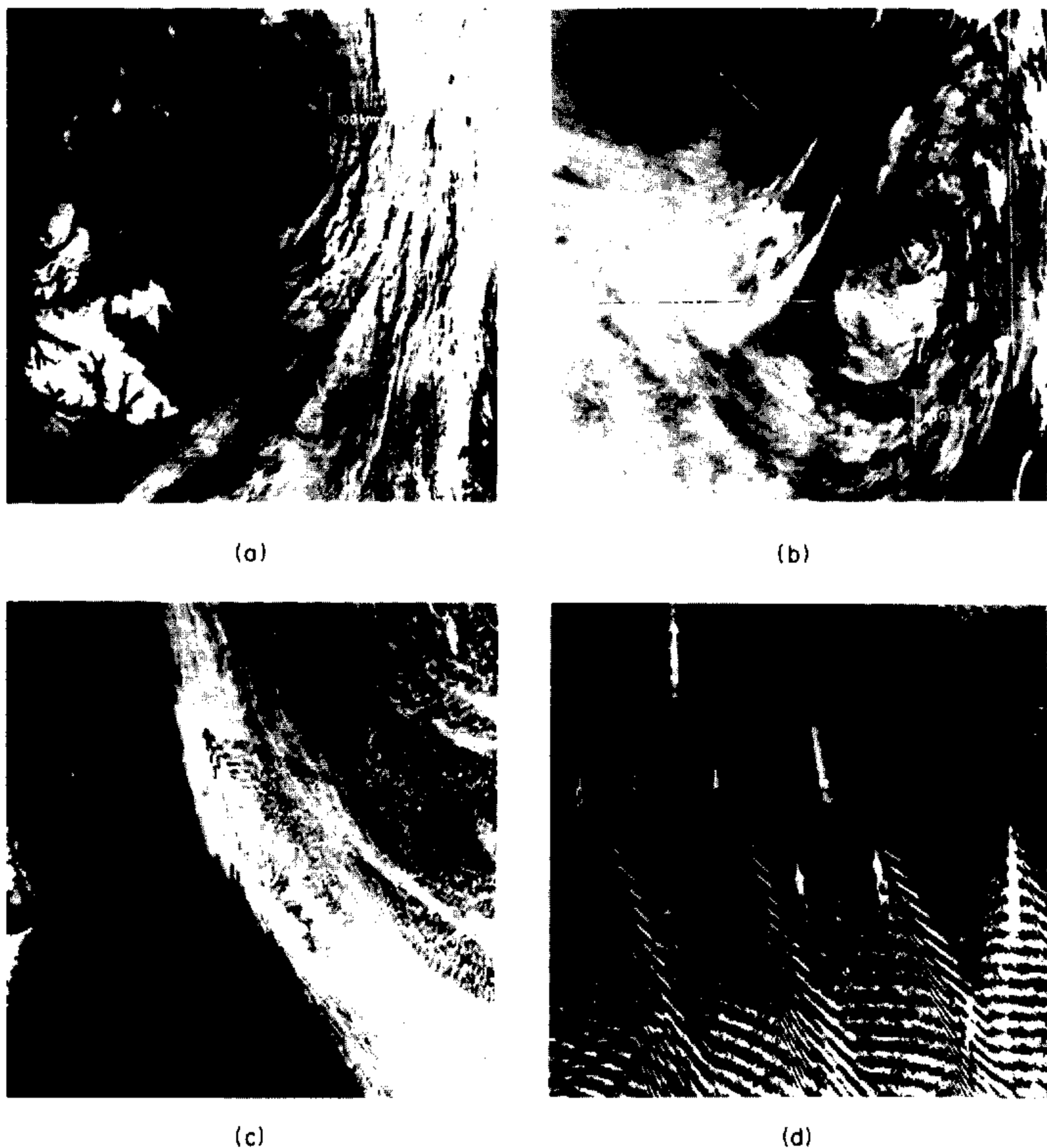
(a)

(b)

(c)

(d)

Figure 7.   Satellite observations of ship-wave patterns over (a) Bear Island, 19 September 1976, (b) Jan Mayen, 8 October 1976, (c) Jan Mayen, 1 September 1976. Plate (d) is from Stoker (1957) and shows the geometric wave patterns generated by a ship moving through deep water.

profiles of N^2 and Richardson number $Ri = N^2 (dU/dz)^{-2}$. The wind and temperature data were obtained from upper air stations on the individual islands and (a), (b), (c) of Fig. 8 are the profile data for the observations in (a), (b), (c) of Fig. 7 and are respectively from (a): Bear Island, 19 September 1976, 1115–1234 GMT; (b): Jan Mayen, 8 October 1976, 1115–1227 GMT; (c): Jan Mayen, 1 September 1976, 1115–1220 GMT. Topographic maps for these islands reproduced in Gjevik and Martinsen demonstrate that they may be represented by the functional form

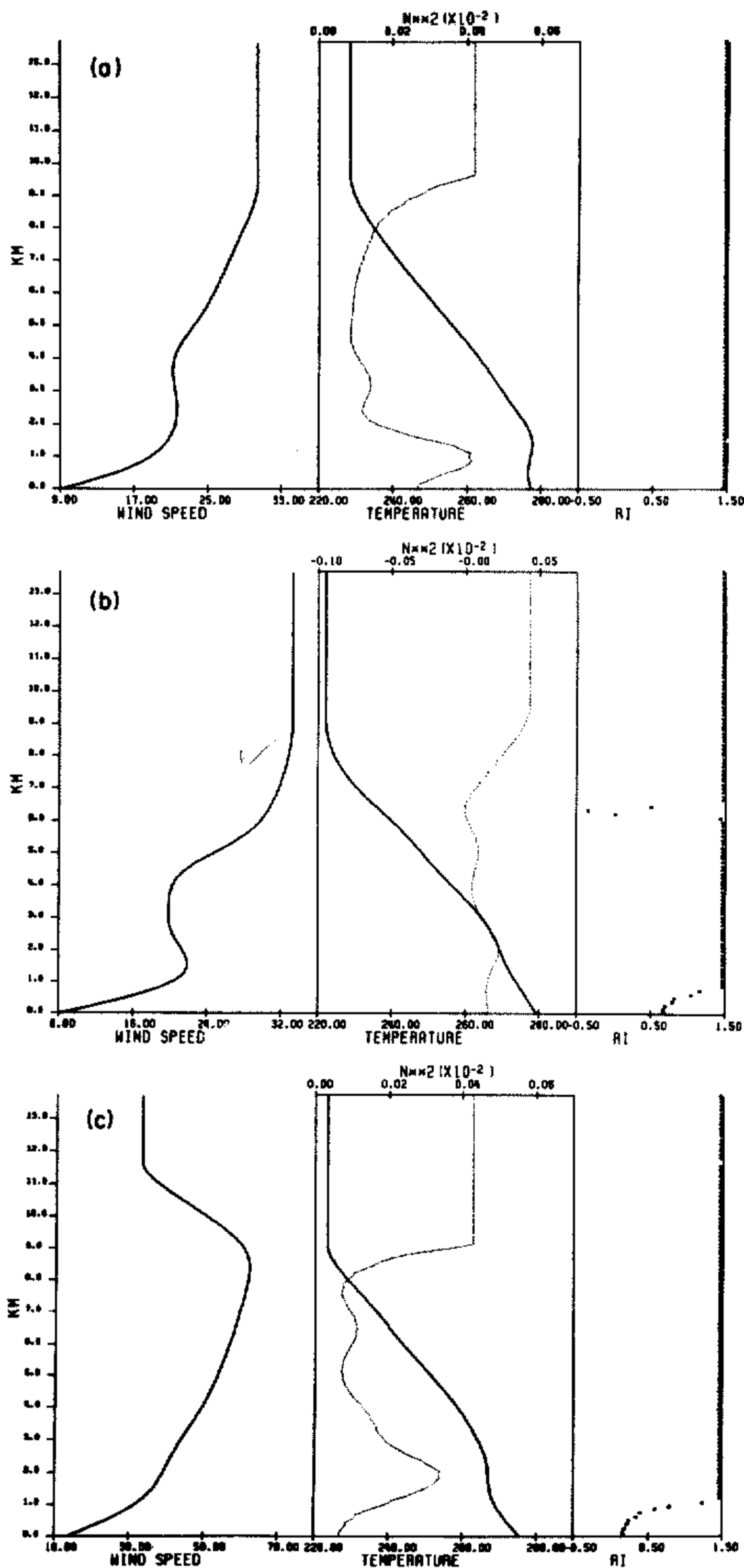$$z_s(x, y) = b^4 h / \{(x^2 + b^2)(y^2 + b^2)\} \tag{27}$$

Figure 8. Environment profiles for (a) Bear Island, 19 September 1976, (b) Jan Mayen, 8 October 1976, (c) Jan Mayen, 1 September 1976. The light line on the central diagram is for the squared Brunt–Väisälä frequency (N^2) while the dark line is for the absolute temperature.

which is of some use in the expression for the linear response since it has an analytic wavenumber spectrum

$$z_s(k, l) = \pi^2 h b^2 \exp\{-(k + l)b\}. \tag{28}$$

The choice $h = 2277\,\text{m}$, $b \simeq 7\cdot5\,\text{km}$ provides a reasonable approximation to the topography of Jan Mayen whereas the choice $h = 300\,\text{m}$, $b = 4\,\text{km}$ is appropriate for Bear Island.

(a) Linear response patterns in three dimensions

The observed response at Bear Island, Fig. 7(a), is dominated by the transverse response component. Figure 9 shows the downstream wave pattern determined from the
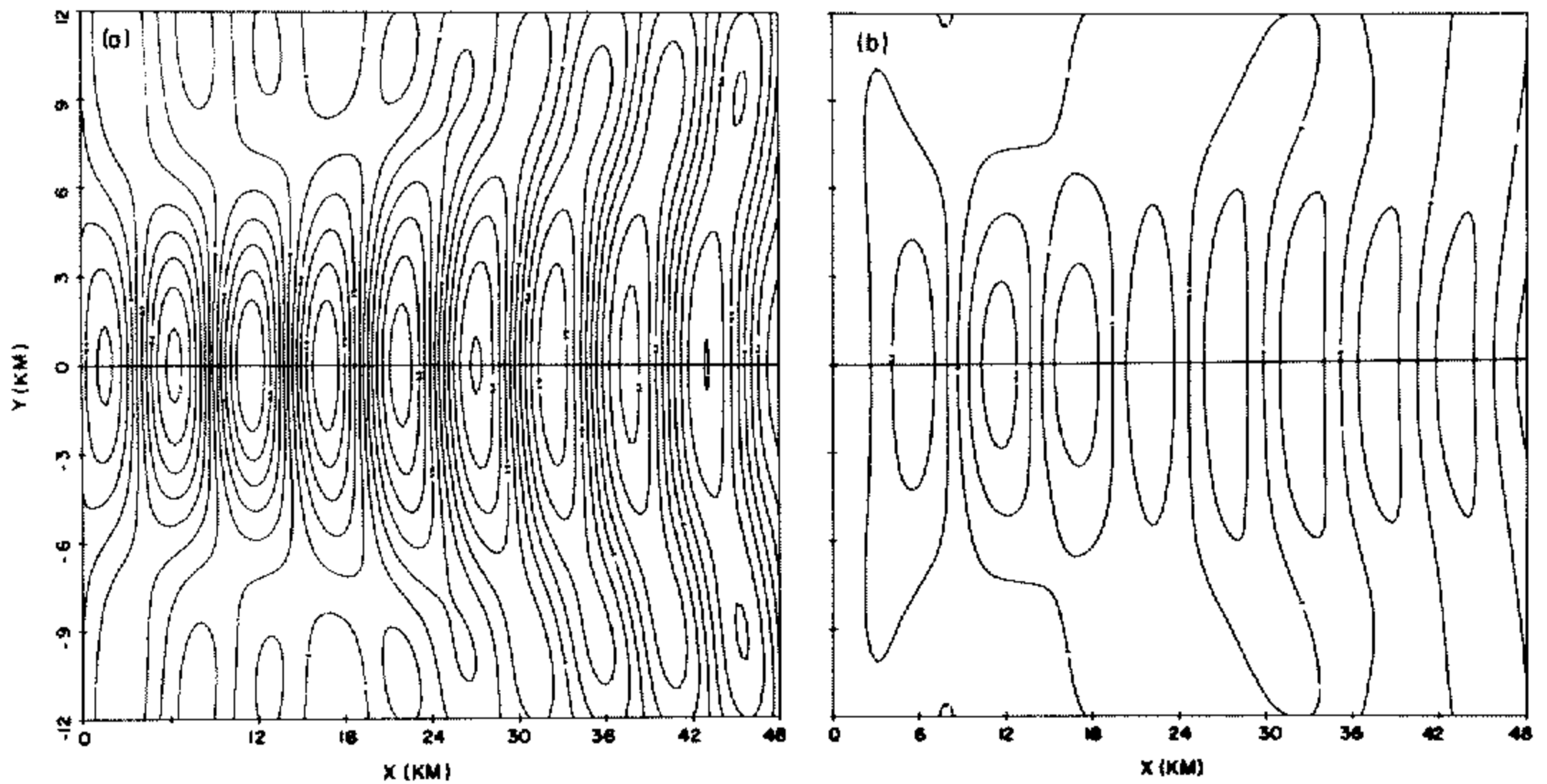

Figure 9.   Planform of the vertical velocity perturbation computed using linear theory for the Bear Island, 19 September 1976. Plate (a) is for a height of 1700 m and plate (b) for a height of 4080 m. The contour interval is $0\cdot2\,\text{m s}^{-1}$.

linear response equation when the background profiles of windspeed and temperature are employed in the calculation. These solutions are plan views of the vertical component of the perturbation wind field (a): at the height $z = 1700\,\text{m}$, which is the height at which the wave amplitude is largest, and (b): at $z = 4080\,\text{m}$. Clearly the wave amplitude falls rapidly with height due to the fact mentioned previously that these disturbances which are periodic in the downstream direction are waves which are trapped in the vertical between the ground and some overhead level of strong partial reflection. They are normal modes of the atmosphere which have zero horizontal phase velocity. Although there is some noise in these low resolution linear solutions (for $-6\,\text{km} < y < 6\,\text{km}$) the main characteristics of the wave field are nevertheless quite clearly revealed. The semi-wedge angle within which the disturbance is confined is about $15°$, in accord with observation, and the transverse wavelength, λ_x, is $\simeq 11\,\text{km}$, which also accords well with satellite observations. It is also useful to note that if one computes the so-called Scorer parameter for this flow from upstream wind and stability profiles using the definition $S_c^2 = N^2/U^2 + (1/U)d^2U/dz^2$, it is found that S_c^2 is a decreasing function of height so that trapped lee waves would be expected in a two-dimensional case. This criterion is therefore able to predict the appearance of the transverse component of the trapped wave spectrum though it is of no use whatever in predicting the existence of the three-dimensional diverging wave patterns which are so prominent in Figs 7(b, c).
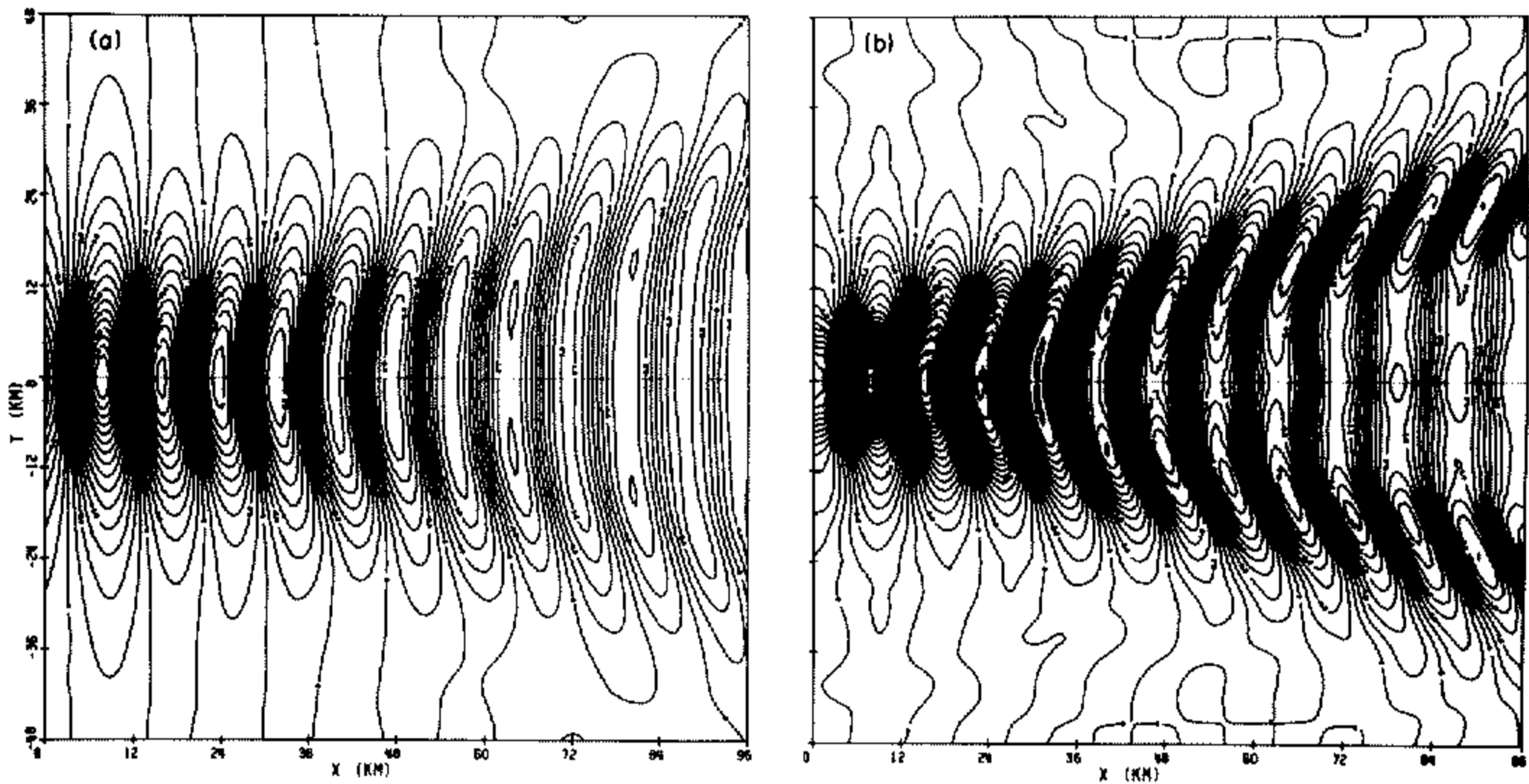
Figure 10. Planform of the vertical velocity perturbation computed using linear theory for Jan Mayen, 8 October 1976. Plate (a) is for a topographic half-width of 7·5 km while plate (b) is for a half-width of 4·0 km. The contour interval is 0·4 m s^{-1}.

Figure 10 shows a plan view of the response pattern predicted by linear theory for Jan Mayen (8 October 1976 event). Figures 10(a) and (b) show the perturbation vertical wind field downstream of the topographic maximum for assumed topographic halfwidths of 7·5 and 4 km respectively. Both computations are for a height $z = 1700$ m, which is again near the height of maximum wave amplitude. Inspection of this figure shows that with broader topography the nature of the response is predominantly transverse whereas with more localized topography the response field is transformed into one dominated by the diverging wave pattern. The fact that the latter is observed on the satellite data in Fig. 7(b) indicates that the effective topographic half-width of the excitation is probably closer to 4 than to 7·5 km. In the observation, individual wave crests make an angle of about 58° with the wind direction and the semi-wedge angle within which the disturbance is confined is about 10° to the north and nearer 23° to the south. The observed wavelength is near 13 km. The theoretically predicted wavelength from linear theory is nearer 16 km, which is reasonable agreement considering that lengths appear foreshortened on the satellite photographs, and the disturbance is confined to a semi-wedge angle of $\sim 10°$ with surfaces of constant phase making an angle of approximately 80° with the wind direction.

Figure 11 shows the vertical perturbation velocity field computed from linear theory for the second observation at Jan Mayen (1 September 1976). Figures 11(a) and (b) again show plan views of wave amplitude at height $z = 1700$ m for topographic half-widths of 7·5 km, (a), and 4 km, (b), as in the last example. In this instance the strongly diverging wave pattern which is characteristic of the response is independent of the topographic half-width. The satellite observation (Fig. 7(c)) shows a wavelength of ~ 13 km and a semi-wedge angle within which the disturbance is confined of $\sim 28°$. Individual wave crests make an angle of $\sim 35°$ with the wind direction near the island but this seems to decrease to nearer 25° further downstream. Inspection of Fig. 11 indicates that in the theoretical solution individual wave crests make an angle of 30°–40° with the wind direction for $b = 4$ km and 35°–45° with the wind direction for $b = 7·5$ km. The theoretical wavelength is near 19 km, which differs considerably from that measured from the satellite photograph. Again, however, the effect of foreshortening on the photograph is extreme so that the agreement is in fact quite acceptable.

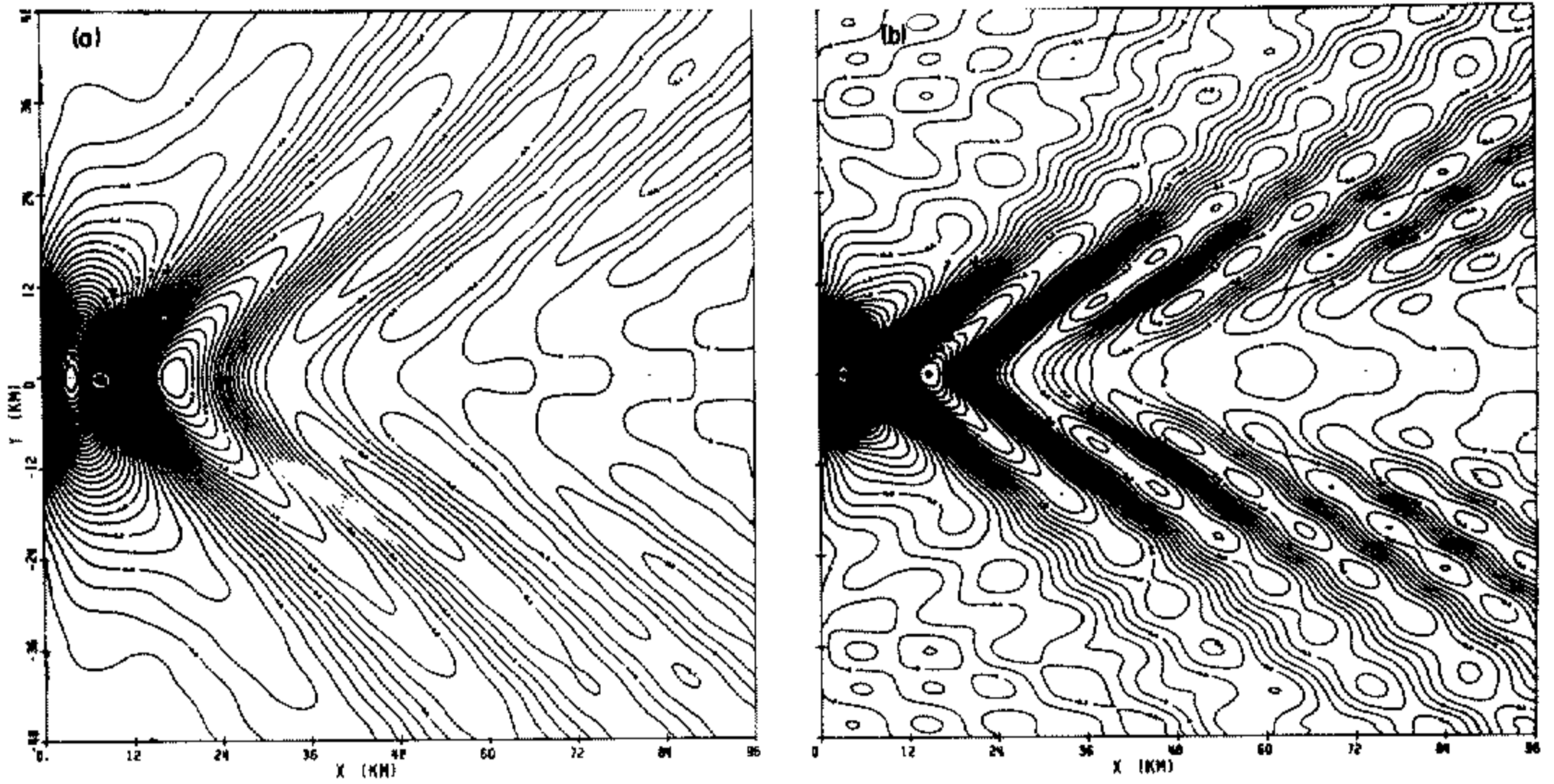On the basis of the comparisons presented above it is quite clear that the linear

Figure 11. Planform of the vertical velocity perturbation computed using linear theory for Jan Mayen, 1 September 1976. (a) is for a topographic half-width of 7·5 km; (b) for a half-width of 4 km. The contour interval is 0·2 m s^{-1}.

theory described in section 2(b) is able to provide a reasonable quantitative simulation of the properties of three-dimensional trapped waves excited by stratified flow over isolated topography. It is furthermore clear on the basis of these comparisons that the geometric wave pattern which dominates the response in such flows is determined by a complicated interplay between the wavenumber spectrum of the topographic forcing and the normal mode spectrum of the stratified waveguide itself. In the next sub-section we will employ the nonlinear model described in section 2(a) to investigate the extent to which nonlinear effects might be expected to alter the nature of the observed field of internal waves.

(b) Nonlinear response patterns in three dimensions

In the two numerical integrations of the full three-dimensional time-dependent non-linear equations to be presented here, we have made explicit use of the fact that for fixed direction of the background wind, and for symmetric topography, the hydrodynamic solutions must be reflection symmetric across a vertical plane oriented in the direction of the mean flow and passing through the topographic maximum. This symmetry, evident in the previously discussed linear results, makes it possible for us to employ half the grid-points in the finite difference model, compared with what would otherwise be required for a given level of resolution. In Fig. 12 we show six time-slices through the evolving planform of the vertical velocity field at height $z = 1700$ m. The model is initialized with the wind and stability profiles corresponding to the Bear Island observations of 18 September 1976, on which occasion the satellite photograph showed a wave field dominated by the transverse response component. The numerical model employed 42 gridpoints in the vertical, 96 gridpoints in the downstream direction, and 28 in the cross-stream direction. The individual time frames in Fig. 12 are separated by 20 min intervals so that the complete sequence covers a two-hour period. Inspection of this figure shows very nicely the manner in which the transverse normal mode is set up as time progresses by the process of successive partial reflection of the internal waves in the body of the fluid and total reflection at the ground. The model topography employed in this calculation was precisely the same as that used for the linear solution shown in Fig. 9(a).

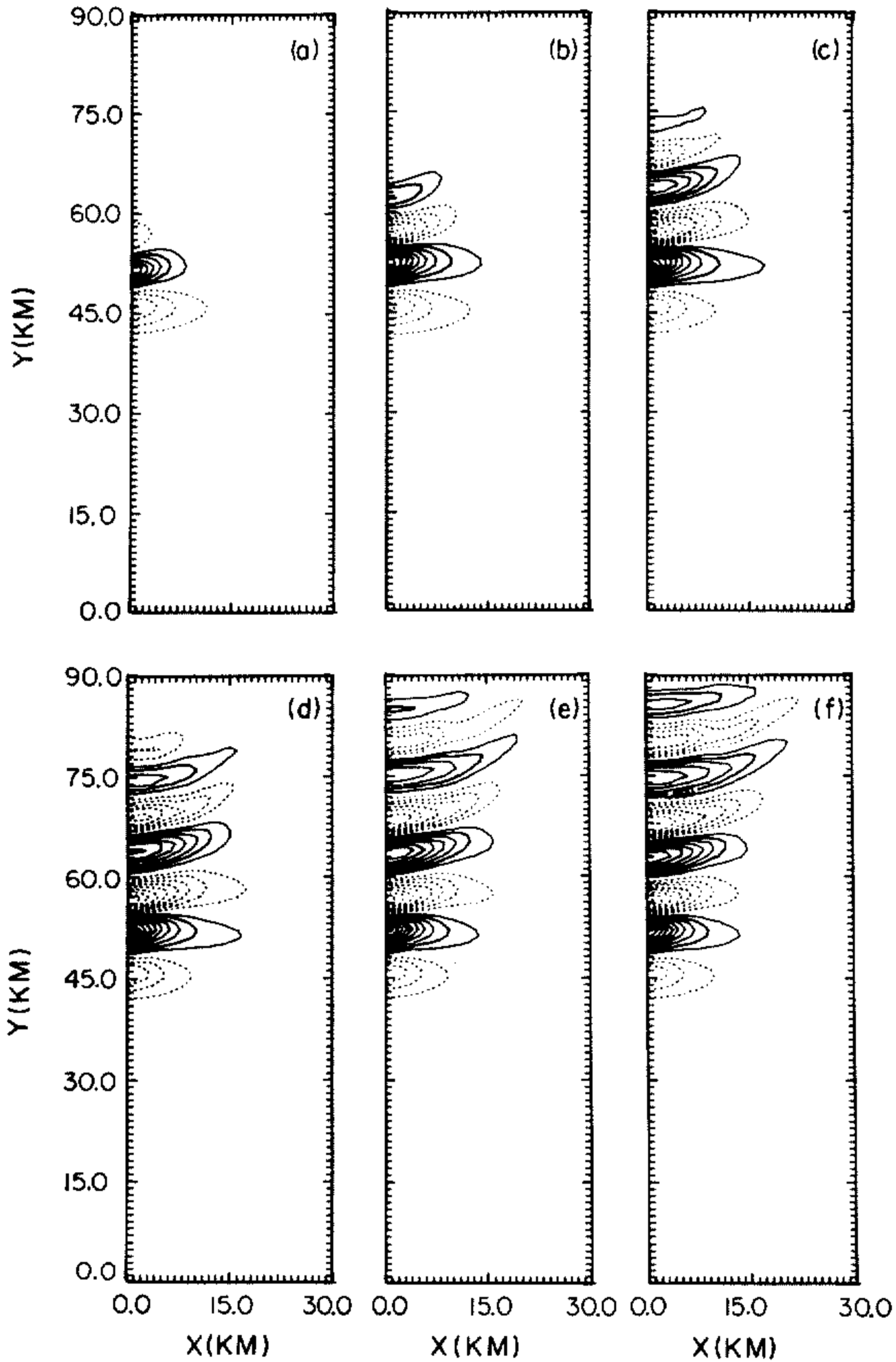Comparing the maximum amplitudes in the first three half wavelengths of the nonlin-

Figure 12. Evolution in time of the planform of the vertical velocity field from the nonlinear model for Bear Island, 19 September 1976. The planforms are at elevation $z = 1700$ m and are shown only for half the full field. The other half is obtained by reflection across the left boundary. Contour interval is 0.25 m s^{-1} and dashed and solid contours are regions of negative and positive values of the field respectively. Times are from 1200 to 7200 s in steps of 1200 s, (a) to (f).

ear wave with the corresponding amplitudes obtained from linear theory, the former are $(-1 \, \text{m s}^{-1}, +2 \, \text{m s}^{-1}, -2 \, \text{m s}^{-1})$ whereas the latter are $(-0.6 \, \text{m s}^{-1}, +1.2 \, \text{m s}^{-1}, -1 \, \text{m s}^{-1})$. Clearly then the amplitude of the nonlinear wave is approximately 100% higher than that predicted by linear theory. This is similar to the result for two-dimensional disturbances found in Peltier and Clark (1979). The reason why linear theory may severely underestimate wave amplitude is that it may effectively employ, through use of the linearized bottom boundary condition, an effective topography which is considerably lower than h. The error is large when the Froude number near the ground $(Fr = hN/U_o)$ is of the order one or greater. Physically this number is just the ratio of the maximum topographic height to the hydrostatic vertical wavelength of the internal waves. Even though the topographic height for the flow over Bear Island is rather modest (300 m), Fr is nevertheless large due to the relatively high stability and low wind speed at the surface. Linear theory is therefore severely in error insofar as the predicted wave amplitudes are concerned but it nevertheless predicts wavephase and wavelength rather well.

In Fig. 13 we show a sequence of vertical cross-sections through the evolving vertical velocity field. This representation of the set up of the three-dimensional trapped wave is very similar to Fig. 23 of Peltier and Clark (1979) showing the same phenomenon in two dimensions. These cross-sections are coincident with the plane of mirror symmetry. Successive downstream phases of the trapped wave are set up as time progresses. An important problem is revealed in these sections which is frequently encountered in the numerical simulation of wave mechanical processes such as those reported here. Visible in the upper third of the domain interior are a sequence of numerical images of the physical trapped wave which is entirely confined to the lower levels of the fluid flow. The upper-level disturbances are produced by the reflection of upward propagating internal wave disturbances at the overhead boundary of the numerical domain. Their vertical extent is on the order of the thickness of the region of high viscosity which we employ to absorb these incident waves. This region of viscous absorption was not particularly effective in the present case because the vertical wavelength of the waves in the upper levels was quite large. In spite of this difficulty, however, the region of the flow which was of physical interest was not visibly disturbed. We found this problem to be extremely pronounced in our attempt to reproduce the observations for 8 October at Jan Mayen. In this case we were unable to afford (because of restricted machine memory) to include in the model the number of vertical levels which would be necessary to prevent contamination of the interior solution by reflections from the overhead boundary. Inspection of Fig. 8(b) shows why this problem was encountered. Because of the high value of the wind speed in the capping layer ($\sim 32 \, \text{m s}^{-1}$) the effective hydrostatic wavelength, U/N, was so large that an extremely thick absorber would have been required to do an effective job in absorbing the incident wave.

This problem was not found to be too severe for the Jan Mayen data on 1 September 1976 because the relatively short vertical wavelength of the waves incident upon the viscous absorber (due to the differing wind and stability profiles) made this region rather more effective. Figure 14 shows a sequence of equispaced time-slices through the evolving planform of the vertical motion field for our nonlinear time-dependent solution at height $z = 1700 \, \text{m}$, which may be compared directly with the equivalent linear solution shown in Fig. 11(a). The agreement between these two solutions is rather good for wavephase and wavelength as the nonlinear model produces a strongly diverging wave response with no hint at all of the transverse component. Comparing Figs. 16(b) and (c) it will be observed that the latter has the topography maximum shifted upstream from its location in the former. In fact the solution in (b) was used to initialize a new model with offset topography in order that we might observe the downstream development of the field of diverging waves under conditions which minimize the effects of boundary proximity. Comparing the amplitude of the nonlinear wave with its linear counterpart we obtain $(-6.4 \, \text{m s}^{-1}, +3 \, \text{m s}^{-1}, -0.6 \, \text{m s}^{-1})$ for the maximum amplitude in the first three half wave lengths of
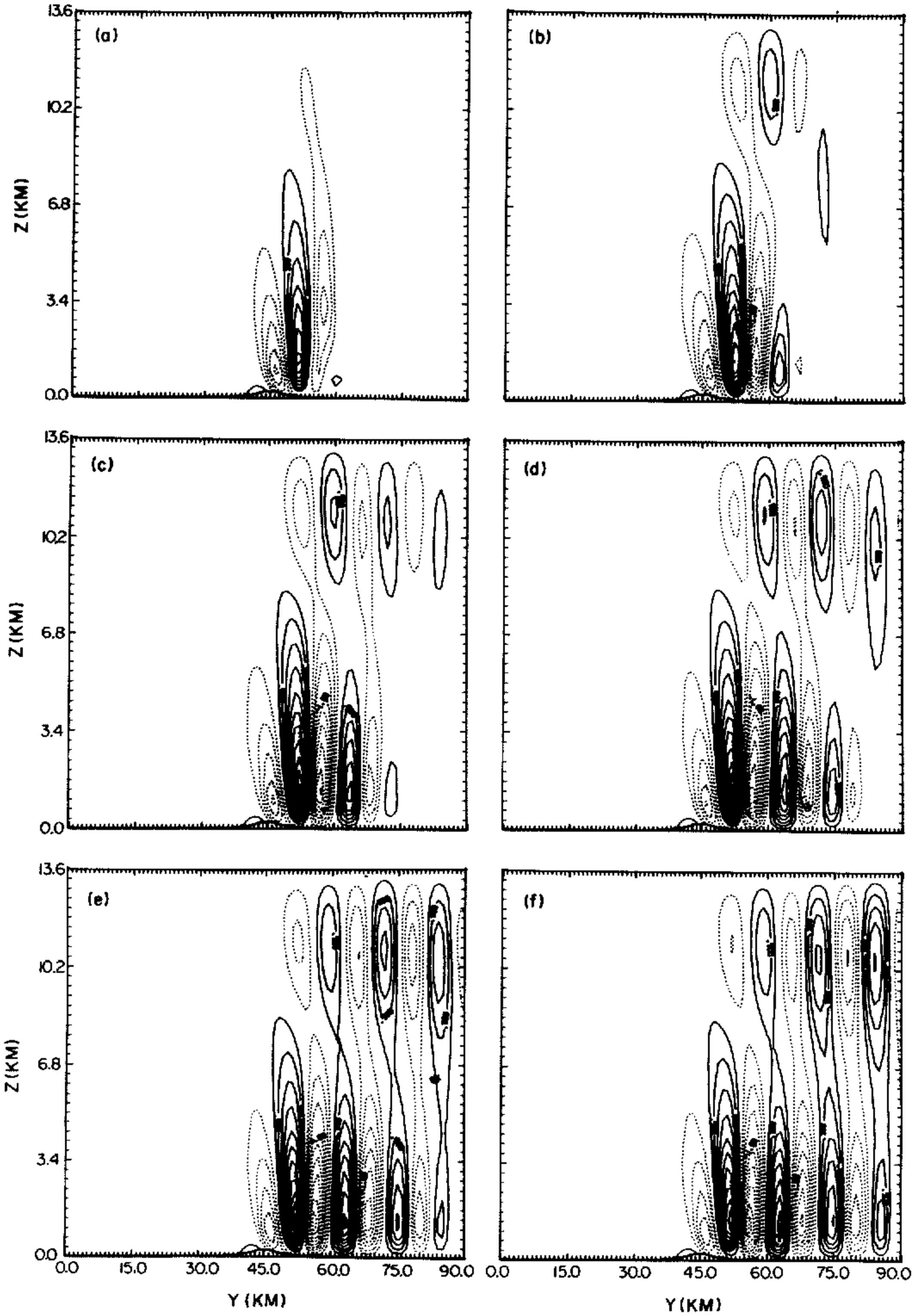
Figure 13. Evolution with time of a vertical section through the vertical velocity field for the Bear Island case. The times are the same as those in Fig. 14. Contour interval is $0.25\,\mathrm{m\,s^{-1}}$ and dashed and solid contours are regions of negative and positive field values respectively.
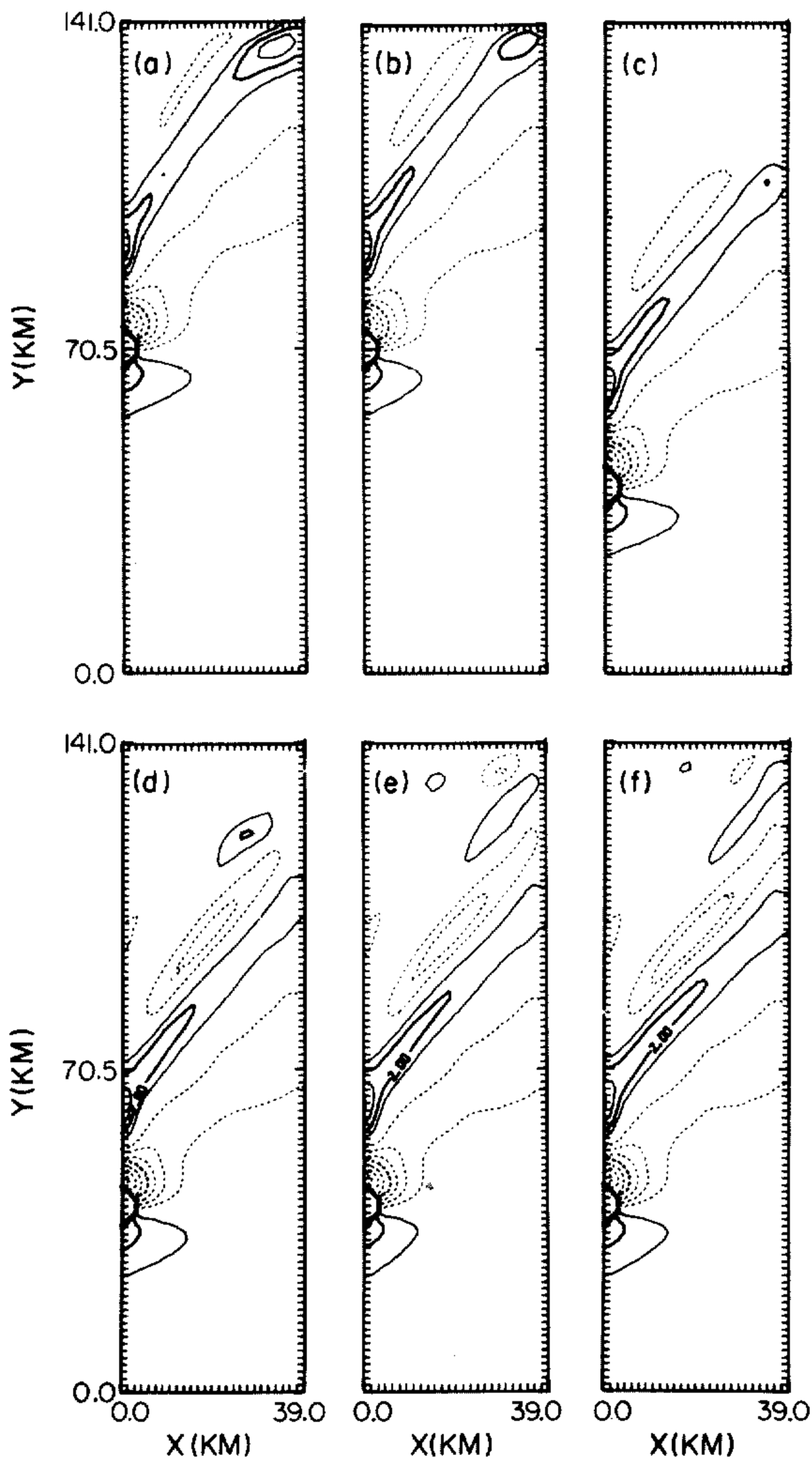
Figure 14. Evolution in time of the half planform of the vertical velocity field at height $z = 1700$ m for Jan Mayen, 1 September 1976. The contour interval on each frame is $1 \, \mathrm{m \, s^{-1}}$ and the times are from 5400 s to 9900 s at 900 s intervals, (a) to (f). Should be compared with the linear steady solution shown in Fig. 13 for the case with topographic half-width 7·5 km.

the latter and $(-8\,\mathrm{m\,s}^{-1}, +3\,\mathrm{m\,s}^{-1}, -1\,\mathrm{m\,s}^{-1})$ for the former. Here then, in contrast to the result obtained for the transverse wave observed in the lee of Bear Island, the linear and nonlinear amplitudes are in quite close agreement. This is in spite of the fact that the maximum topography of Jan Mayen ($\sim 2\cdot 28\,\mathrm{km}$) is very much in excess of that of Bear Island ($\sim 300\,\mathrm{m}$). Again the reason for the good fit in this case is to be found in the rather small value of the Froude number $Fr = hN/U_o$ which obtains (by inspection of Fig. 10(c)) because of the small value of N in the near-surface region.

5. Conclusions

The set of two-dimensional experiments described in section 3 for stratified flow with constant Brunt–Väisälä frequency N and wind speed U have strongly reinforced our opinion, that wave breaking has an important impact on the evolution of the standing wave field over isolated topography. Even in this simplest possible two-dimensional case it has been shown that when the standing wave exceeds the critical steepness the wave begins to amplify in the cavity which forms between the level of supercritical steepening and the earth's surface. By this process downslope wind speeds in the lee of the topographic maximum may reach values several times greater than those which would be predicted by a steady state model of the type introduced by Long. As suggested in Peltier and Clark (1979), we believe that this new mechanism may play an important role in the formation of severe downslope windstorms. The data collected during the course of the ALPEX experiment may help to confirm or to deny this hypothesis.

The sequence of comparisons of linear and nonlinear calculations for three-dimensional flow over isolated topography has served as a very useful check on the design of the three-dimensional numerical model. Both models, linear and nonlinear, were able to reproduce quite accurately the ship-wave patterns observed in the satellite photographs. The geometrical form of the ship-wave pattern may be dominantly transverse or dominantly divergent; which of these patterns actually appears involves a complex interaction between the normal mode spectrum of the waveguide and the spectrum of the topographic forcing. A prediction of the expected response cannot be made purely on the basis of a wave kinematic analysis of the type described in Gjevik and Marthinsen (1978) based on the dispersion relation for the background state. Our linear calculations for the 8 October 1976 observations at Jan Mayen, for example, show quite clearly that the nature of the response may change quite dramatically when the topographic half-width is changed only slightly while the mean flow is kept the same. This is not unexpected. Comparisons of the linear and nonlinear results also demonstrated that the validity of linear theory essentially depends upon the ratio of the topographic height, h, to the hydrostatic wavelength, U/N, as is found to be the case for two-dimensional flows.

References

Bretherton, F. P.   1969   Momentum transport by gravity waves. *Quart. J. R. Met. Soc.*, **95**, 213–243.

Buzzi, A. and Tibaldi, S.   1978   Cyclogenesis in the lee of the Alps. A case study. *ibid.*, **104**, 271–288.

Clark, T. L.   1977   A small scale numerical model using a terrain following coordinate system. *J. Comput. Phys.*, **24**, 186–215.

Clark, T. L. and Peltier, W. R. 1977 On the evolution and stability of finite amplitude mountain waves. *J. Atmos. Sci.*, **34**, 1715–1730.

Gjevik, B. and Marthinsen, T. 1978 Three-dimensional lee wave pattern. *Quart. J. R. Met. Soc.*, **104**, 947–957.

Klemp, J. B. and Lilly, D. K. 1975 The dynamics of wave induced downslope winds. *J. Atmos. Sci.*, **32**, 320–339.

Landau, L. D. and Lifshitz, E. M. 1960 *Mechanics*, Pergamon Press, New York.

Lilly, D. K. 1972 Wave momentum flux – a GARP problem. *Bull. Amer. Meteor. Soc.*, **53**, 17–23.

Marthinsen, T. 1980 Three-dimensional lee waves. *Quart. J. R. Met. Soc.*, **106**, 569–580.

Miles, J. W. and Huppert, H. E. 1969 Lee waves in a stratified flow. Part 4. Perturbation approximations. *J. Fluid Mech.*, **35**, 497–525.

Orlanski, I. 1976 A simple boundary condition for unbounded hyperbolic flows. *J. Comput. Phys.*, **21**, 251.

Peltier, W. R. and Clark, T. L. 1979 The evolution and stability of finite amplitude mountain waves. Part II: surface wave drag and severe downslope windstorms. *J. Atmos. Sci.*, **36**, 1498–1529.

1980 Reply to comments by D. K. Lilly and J. B. Klemp on 'The evolution and stability of finite amplitude mountain waves'. *ibid.*, **37**, 2122–2125.

Sawyer, J. S. 1959 The introduction of the effects of topography into methods of numerical forecasting. *Quart. J. R. Met. Soc.*, **85**, 31–43.

Simard, Angèle and Peltier, W. R. 1982 Ship waves in the lee of isolated topography, *J. Atmos. Sci.*, **39**, 587–609..

Steinacker, R. 1979 *Möglichkeiten synoptischen analysen mit dem derzeitigen Beobachtungsnetz.* Inst. Meteoral. Innsbruck.

Stoker, J. J. 1957 *Water Waves*, Pure and Applied Mathematics, Vol. IV, Interscience Publishers Inc.